BISMUTH OXYCHLORIDE NANOSHEETS MODIFIED WITH Au-Cu NANOPARTICLES FOR EFFICIENT PHOTOREDUCTION OF CO$_2$ TO ETHANE

Xia Zou[a], Sisi Wang[a], Xingxing Zheng[a] and Jun Yang[a],*,[iD]

[a]Department of Chemistry, College of Chemistry and Material Science, Jinan University, 510632 Guangzhou, China

Article

BiOCl nanosheets modified with AuCu nanoparticles were successfully designed and fabricated for water reduction of CO$_2$. The Au$_x$Cu$_y$/BiOCl composites exhibited enhanced visible light absorption ability due to a surface plasmon resonance (SPR) effect. The Au$_x$Cu$_y$/BiOCl composites could convert carbon dioxide to ethane (C$_2$H$_6$), while only CO was obtained over pure BiOCl nanosheets. In this study, the rate of C$_2$H$_6$ production (12.2 µmol h^{-1} g^{-1}) and selectivity of C$_2$H$_6$ (75.7%) were obtained over the Au$_1$Cu$_1$/BiOCl photocatalyst under simulated sunlight illumination. The AuCu nanoparticles played the dual role of electron traps and hot electron donors, facilitating efficient separation and migration of the carriers. The photocatalyst exhibited steady photocatalytic activity over the test duration of 9 h.

Keywords: BiOCl; photocatalysis; photocatalytic CO$_2$ reduction; AuCu nanoparticles.

INTRODUCTION

The increasing level of global industrialization has exacerbated the emission of carbon dioxide, and the large-scale combustion of fossil fuels such as coal and oil has caused serious threat to the human environment.[1] In 2020, China put forward the "double carbon" goal of "carbon peak" and "carbon neutrality", which is an important strategy to solve the prominent problem of resource and environmental constraints. Scientists are seeking ways to decrease the concentration of CO$_2$ in nature, such as converting CO$_2$ into worthy fuels and valuable chemicals. The full conversion and effective treatment of CO$_2$ are crucial tasks.[2] The specific measures to achieve the "dual carbon" goal are not only to directly reduce CO$_2$ emissions but also to convert CO$_2$ as a rich C$_1$ resource into chemicals with higher added value, as an effective approach to sustainability. The photoreduction conversion process of CO$_2$ and H$_2$O using semiconductors is green, economical and clean. It uses inexhaustible solar energy and the H$_2$O in nature as energy and proton sources, which can greatly reduce greenhouse gas emissions and achieve carbon neutrality.[3] To date, in the CO$_2$ photoreduced process, CO and CH$_4$ are mainly generated; there are few studies on the production of C$_{2+}$ products during this reduction process.[4] Among the various CO$_2$ reduction products, C$_{2+}$ products have attracted much attention compared to C$_1$ products because of the characteristics of high energy density and high added economic value. However, due to the different and complex electron transfer pathways involved in CO$_2$ photocatalytic reduction, it remains a challenge to selectively convert CO$_2$ into higher-level carbon species, such as ethane.[5] There are many factors, such as the surface architecture and band gap width of the photocatalyst, as well as whether it can provide an effective catalytic active site and charge transfer channel, that affect the catalytic performance of C$_{2+}$. How to regulate the selectivity of C$_{2+}$ products is an important direction for research in the field of energy.[6] Therefore, the construction of photocatalysts with effective charge separation efficiency to achieve regulatable photocatalytic reduction of CO$_2$ to C$_{2+}$ products is very important.

As a new two-dimensional semiconductor nanomaterial, BiOCl has enormous research potential due to its unique structural advantages. BiOCl is a layered PbFCl-type tetragonal structure, with

[Cl-Bi-O-Bi-Cl] layers stacked by Van der Waals forces. Four O atoms and four Cl atoms in the layer combine with one Bi atom through chemical bonds, resulting in a square antiprism structure, presenting an alternating arrangement of Cl$^-$/[Bi$_2$O$_2$]$^{2+}$ bilayers. Therefore, layered structures can induce the formation of internal electric fields along the (001) direction, providing abundant space for polarized atoms and atomic orbitals, which helps to induce dipole moments to separate electrons and holes.[7] Its unique structure facilitates the separation of photogenerated charge carriers, thereby promoting electron migration to surface active sites and accelerating catalytic reactions, making it a promising material for the photocatalytic reduction of CO$_2$. At present, there is a large body of research applying BiOCl to the field of photocatalysis, demonstrating good photocatalytic performance for various photocatalytic reactions. However, there are few studies on the use of BiOCl for the photocatalytic reduction of CO$_2$.[8]

Very recently, Wang *et al.*[9] found that CO$_2$ can be efficiently converted into ethane (C$_2$H$_6$) over bismuth-rich bismuth oxybromide nanotubes (Bi$_1$$_2O_1$$_7Br_2$) modified with gold nanoparticles. Bimetallic nanoparticles show different electrical, chemical, optical, and other characteristics compared to single metal nanoparticles due to the synergistic effect between metals. Especially in the field of catalysis, they show better performance.[10-12] The synergistic effect of bimetallic nanoparticles is crucial for achieving effective catalytic cycling. Metal particles can help photogenerated electrons diffuse faster to the surface of catalysts and act as acceptors, reducing the probability of electron-hole recombination. Therefore, compared to single metal nanoparticles, different bimetals, such as gold platinum bimetallic,[13-15] gold copper bimetallic,[16] gold palladium bimetallic,[17,18] and gold silver bimetallic nanoparticles,[19-21] have better catalytic performance in highly concerned photocatalytic reactions. Compared to Au or Cu monometallic photocatalysts, it was reported that AuCu bimetallic nanoparticles have stronger photocatalytic activity during CO$_2$ reduction.[22-24] Previous studies have shown that the generation efficiency of thermal holes and electrons in catalysts is the key to improving photocatalytic efficiency. Photocatalytic materials composed of plasmonic noble metal nanoparticles and semiconductor materials can effectively extract and collect thermal holes, stimulating more electrons and holes.[25-27] In addition, Sato *et al.*[28] found that the photocatalyst composed of AuCu core-shell nanoparticles and titanium oxide support shows significantly improved activity because

*e-mail: tyangj@jnu.edu.cn

of the SPR effect between bimetallic plasmonic photocatalysts. Although photocatalysts with bimetallic nanoparticle structures have been extensively reported, little has been done to influence the selectivity of photocatalytic CO_2 reaction to produce C_{2+} products by adjusting the bimetallic ratio.

Here, we establish a photoinduced deposition method to synthesize bimetallic AuCu nanoparticle-decorated BiOCl (BOC) nanosheets. Compared to Cu/BiOCl or Au/BiOC, Au_1Cu_1/BiOCl composite materials show higher photocatalytic performance for CO_2 reduction under sunlight (AM 1.5 G) irradiation.

EXPERIMENTAL

Reagents and solutions

Bismuth nitrate pentahydrate $Bi(NO_3)_3.5H_2O$ (99%), potassium chloride, $CuCl_2.2H_2O$ (99.9%), $HAuCl_4.3H_2O$ (99.9%), and ethanol were purchased from Shanghai Chemical Reagents Co., Ltd. This experiment used deionized water (18.2 MΩ cm). The reagents used in the experiment were used directly without treatment, unless otherwise stated.

Material fabrication

BiOCl was prepared using the hydrothermal method. First, 0.002 mol $Bi(NO_3)_3.5H_2O$ and 0.002 mol KCl were added to 30 mL of a mixed solution of water and ethanol (ethanol:water, 1:1). After stirring for 30 min, we transferred this solution to a 100 mL Teflon-lined autoclave and maintained it at 120 °C for 8 h. After the reaction was completed, it was cooled to room temperature, centrifuged at 8000 r min^{-1}, and washed four times with water and ethanol, respectively. Lastly, we dried the sample at 60 °C for 12 h.

A series of BiOCl photocatalysts modified with Cu-Au NPs were obtained by a stepwise photoreduction deposition method. Typically, 0.15 g of BiOCl nanosheet was added to 40 mL of deionized water and subjected to ultrasonic treatment for 10 min. Under intense stirring, different amounts of $HAuCl_4$ solution (5.0 g L^{-1}) were added dropwise to the mixed solution. Then, the solution was stirred and irradiated under a Xenon lamp (500 W) for 30 min. Similarly, different amounts of $CuCl_2.2H_2O$ solution (5.0 g L^{-1}) were added dropwise to the mixed solution and irradiated for another 30 min. Eventually, the sample was centrifuged at 8000 r min^{-1} and was washed with deionized water four times. The resulting sample was dried at 60 °C for 12 h. The total Au and Cu content of Au_xCu_y/BiOCl was fixed at 2 wt.%, where x and y are the content of Au and Cu, respectively. Au/BiOCl, $Au_{1.6}Cu_{0.4}$/BiOCl, Au_1Cu_1/BiOCl, $Au_{0.4}Cu_{1.6}$/BiOCl, and Cu/BiOCl photocatalysts were obtained by adding variable amounts of aqueous $HAuCl_4.3H_2O$ and $CuCl_2.2H_2O$ solutions.

Characterization

The X-ray power diffraction (XRD) was analyzed via a Bruker D8 Focus X-ray diffractometer (Bruker, Mannheim, Germany) with Cu-Kα radiation (λ = 0.154178 nm). Transmission electron microscopy (TEM) and high-resolution TEM (HRTEM) were performed using a transmission electron microscope (JEM-2100F, Kyoto, Japan). The UV-Visible diffuse reflectance spectra of the samples were acquired using a UV-Vis spectrophotometer (Cary4000, Agilent, Petaling Jaya, Malaysia). X-ray photoelectron spectroscopy (XPS) was performed via an ESCALAB 250 spectrometer (Thermo Fisher Scientific, Waltham, MA, USA) with an Al-Kα (1486.6 eV) line to obtain the elements and chemical state. The photoluminescence (PL) emission spectra were measured

on a RF-5301PC fluorescence spectrophotometer (Shimadzu, Kyoto, Japan). The measurement of photocurrent reaction and electrochemical impedance spectroscopy (EIS) were carried out using a traditional three-electrode system with a 0.1 M Na_2SO_4 electrolyte solution on an electrochemical system (CHI 760, Shanghai, China).

Photocatalytic test

The catalyst (5.0 mg) was added to deionized water (400 μL) and then treated with ultrasound to form a suspension, which was dispersed on the surface of a 3.5 cm glass slide. After drying, we placed the slide in the bottom of a 135 mL reaction chamber and added 100 μL of deionized water to the reactor to provide a hydrogen source. Next, we sealed the reactor with a transparent quartz lid and ventilated it with pure CO_2 (99.9%) for 15 min. Lastly, the reactor was irradiated by simulated sunlight (PLS-SXE300D), with nearly 200 mW cm^{-2} light intension. The gaseous sample was taken out every hour and examined by gas chromatography (Shimadzu, GC-2014A) using a conductivity detector (TCD) and a flame ionization detector (FID). The selectivity of products was calculated using the equations shown below:

$$S_{C_2H_6} = 14RC_2H_6 / \left(2RCO + 8CH_4 + 14RC_2H_6\right) \times 100\% \qquad (1)$$

$$S_{C-H} = \left(14RC_2H_6 + 8RCH_4\right) / \left(14RC_2H_6 + 8RCH_4 + 2RCO\right) \times 100\% \quad (2)$$

where $S_{C_2H_6}$ and S_{C-H} represent the selectivity of ethane and alkane (ethane and methane), respectively.

RESULTS AND DISCUSSION

The crystalline phases and compositions of the prepared BiOCl, Au/BiOCl, Cu/BiOCl, and Au_xCu_y/BiOCl were detected by XRD (Figure 1). The XRD peaks of BiOCl were well indexed to the tetragonal structure of BiOCl (JCPDS No. 06-0249). After the deposition of Au and Cu, the diffraction peaks of BiOCl (JCPDS No. 06-0249) were found in the XRD patterns of all catalysts, reflecting that Au and Cu nanoparticles were only deposited on the surface of the catalyst without affecting the crystalline phase of BiOCl. However, no diffraction peaks of Au and Cu were observed in Au_xCu_y//BiOCl due to its low loading counts and uniform dispersion.

The elemental compositions of the surfaces were detected by X-ray photoelectron spectroscopy (XPS). It can be found that the presence
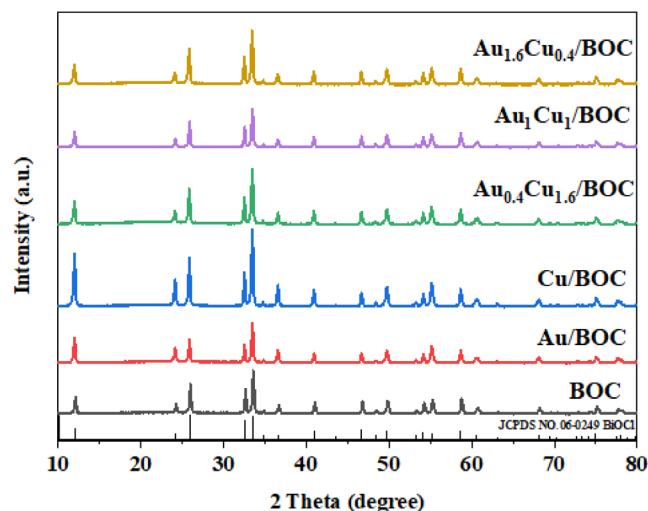

Figure 1. *XRD patterns of BiOCl, Au/BiOCl, Cu/BiOCl, and AuxCuy/BiOCl photocatalysts*

of Cl, O, and Bi was visibly present in the complete XPS spectra (Figure 2a). Compared to the XPS peaks of the pure BiOCl sample, the Bi 4f (Figure 2b), O 1s (Figure 2c), and Cl 2p (Figure 2d) XPS peaks of Au/BiOCl, Au$_1$Cu$_1$/BiOCl, and Cu/BiOCl all underwent a binding energy shift; the loading of AuCu particles on the BiOCl nanosheets may have affected the charge transfer on the catalyst surface and, in turn, the relationship between the BiOCl nanosheets and AuCu nanoparticles.

The two peaks corresponding to the Au^0 species in the Au/BiOCl composites are at 83.6 and 87.3 eV in Figure 2e, while the characteristic peaks of the Cu^0 species in the Cu/BiOCl

composites are at 932.4 and 952.2 eV in Figure 2f. In the case of the Au$_1$Cu$_1$/BiOCl composite, the binding energy of Au 4f shifts towards the high energy level, and the peak of Cu 2p shifts negatively towards lower energies.[29,30] Cu^0 is prone to oxidation at room temperature, while the oxidation state of Au generally does not change.[31,32] The main characteristic peaks at 931.9 and 951.7 eV belong to Cu 2p$_{3/2}$ and Cu 2p$_{1/2}$ of metal Cu^0 or Cu$^+$, while the main characteristic peaks at 84.0 and 87.7 eV belong to Au 4f$_{7/2}$ and Au 4f$_{5/2}$ of metal Au^0. Due to the overlapping XPS peaks of Cu$^+$ and Cu^0, in order to distinguish the chemical valence states of copper, the Cu LMM Auger narrowing
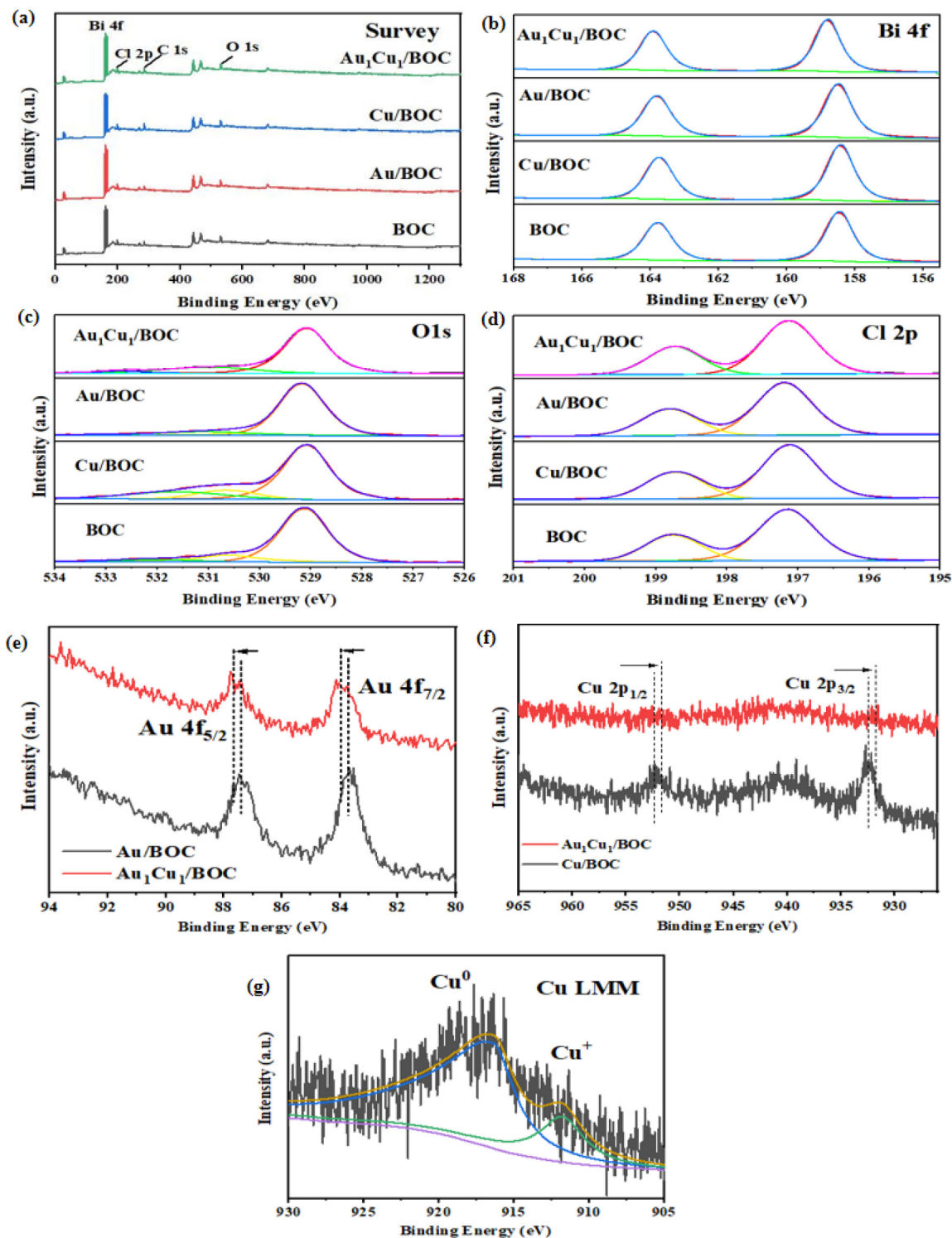

Figure 2. XPS spectra for full-spectrum scanning survey (a); Bi 4f (b); O 1s (c); Cl 2p (d); Au 4f (e); Cu 2p (f), and Cu LMM Auger (g) of the photocatalysts

of the Au_1Cu_1/BiOCl composite material was tested. Figure 2g shows a wide and asymmetric peak, which is deconvoluted into two peaks at 911.9 and 916.8 eV, corresponding to Cu^+ and Cu^0, respectively.[33,34] In Au_1Cu_1/BiOCl composite materials, the interaction between AuCu and BiOCl causes Au^0 to lose electrons, which then migrate to Cu^0. When Au_1Cu_1/BiOCl composites are irradiated under visible light, the catalyst can effectively absorb photons as well as excite and generate electrons.[35] The excited-state electrons continuously accumulating in the Au site are eventually transferred to the Cu site due to charge rebalancing,[36] which improves the transmission and separation speed of electrons in Au_1Cu_1/BiOC composites.

The microscopic morphology of Au_1Cu_1/BiOCl was detected by scanning electron microscopy (SEM) and transmission electron microscopy (TEM). Figures 3a and 3b, SEM show the morphology of BiOCl catalyst is thin nanosheets and the deposition of Au and Cu did not significantly alter the architecture of the BiOCl nanosheets. Additionally, Figures 3c and 3d show that the photoreduced Au and Cu nanoparticles were mainly deposited on the surface of the BiOCl nanoparticles. As shown in Figure 3f, the (110) lattice plane corresponding to BiOCl has a lattice plane spacing of 0.28 nm. The high-resolution transmission electron microscopy (HR-TEM) image clearly shows two clear lattice plane spacings (0.24 and 0.22 nm) of the AuCu (JCPDS 38-0741), corresponding to the (211) and (201) lattice planes, respectively. Figure 3e shows that the size of the AuCu particles deposited on the surface of the BiOCl nanoparticles is approximately 18 nm. Figures 3g-3l show that the elements of Bi, O, Cl, Au, and Cu in the energy dispersive X-ray spectroscopy (EDS) are equably distributed in Au_1Cu_1/BiOCl.

To make clear the prominent CO_2 photocatalytic reduction performance of Au_1Cu_1/BiOCl, electrochemical experiments were conducted. As shown in Figure 4a, Au_1Cu_1/BiOCl exhibits a stronger photocurrent response than BiOCl, Cu/BiOCl, and Au/BiOCl, suggesting that Au_1Cu_1/BiOCl has better electron and hole pair separation efficiency. In addition, the interfacial charge transfer characteristics of BiOCl, Cu/BiOCl, Au/BiOCl, and Au_1Cu_1/BiOCl were studied *via* electrochemical impedance spectroscopy (EIS)

(Figure 4b). Au_1Cu_1/BiOCl has the smallest arc radius. In general, the smaller the arc radius displayed by photocatalysts, the smaller the electron transfer resistance. Au_1Cu_1/BiOCl has the smallest arc radius, reflecting a favorable surface charge transfer speed on the surface of the photocatalyst.[37] Time-resolved fluorescence emission attenuation spectroscopy was used to further study the material. The average fluorescence lifetime of pure BiOCl is slightly higher than that of Au_1Cu_1/BiOCl, possibly due to the efficient photogenerated charge transfer speed (Figure 4c). In conclusion, the introduction of AuCu nanoparticles onto the surface of BiOCl nanosheets helps to accelerate the diffusion of photogenerated electrons to the catalyst surface, inhibits the recombination rate of electrons and holes, and allows more photogenerated electrons and holes to participate in subsequent reactions, greatly improving the catalyst's activity.

Figure 5a records the UV-Visible absorption spectrum of BiOCl, Au/BiOCl, Cu/BiOC, and Au_1Cu_1/BiOCl, indicating the light absorption characteristics of the catalysts. In Figure 5a, it can be seen that a series of photocatalysts exhibited strong spectral absorption peaks between 300 and 500 nm. In addition, compared with other photocatalysts, due to the special local surface SPR effect of AuCu nanoparticles, the spectral absorption peak of Au_1Cu_1/BiOCl shifted at a longer wavelength and had a great response to visible light at 480 nm, reflecting that AuCu nanoparticles were successfully loaded onto BiOCl nanosheets. The band gap (Eg) of the BiOCl nanosheets was close to 3.56 eV according to the Tauc method (Figure 5b) and the band gap (Eg) of the Au_1Cu_1/BiOCl was close to 3.13 eV.[38] The equation is as follows.

$$(\alpha h\nu)^n = B(h\nu - E_g) \tag{3}$$

where α, h, ν, Eg, and B are the absorption coefficient, Planck's constant, vibrational frequency, band gap, and a constant, respectively. For direct and indirect semiconductors, n is 1/2 and 2, respectively.[39]

In order to obtain the flat band voltage of BiOCl and Au_1Cu_1/BiOCl, the Mott-Schottky curve was measured at 500, 800, and 1000 Hz, respectively. From Figure 5c, it can be seen that the slope
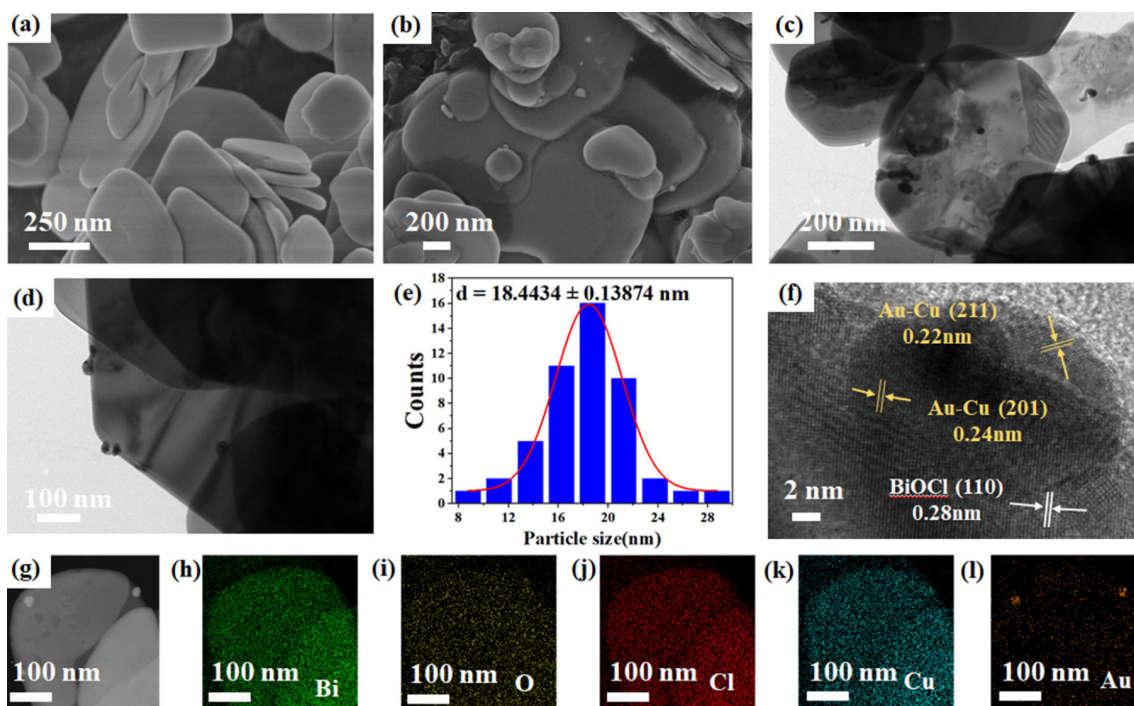
Figure 3. *SEM image (a) of BiOCl, SEM image (b) of Au_1Cu_1/BiOCl, TEM images (c-d), particle size distribution diagram (e), HR-TEM image (f) and elemental mapping images (g-l) of Au_1Cu_1/BiOCl*
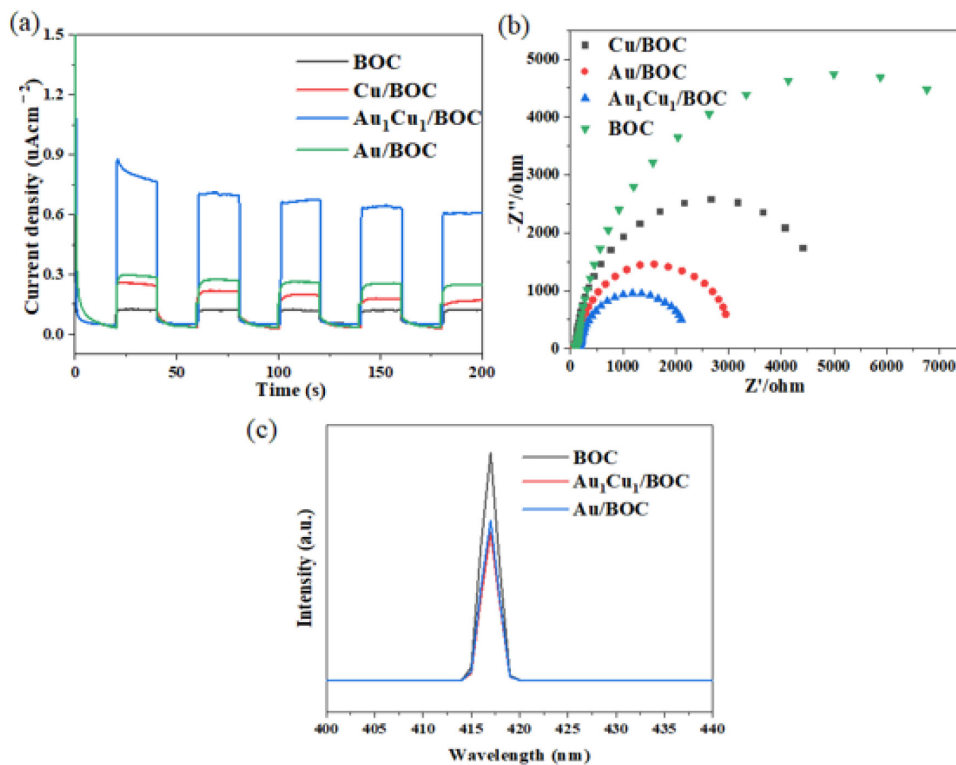
Figure 4. *(a) Transient photocurrent spectra, (b) EIS spectra, and (c) PL spectra of samples*
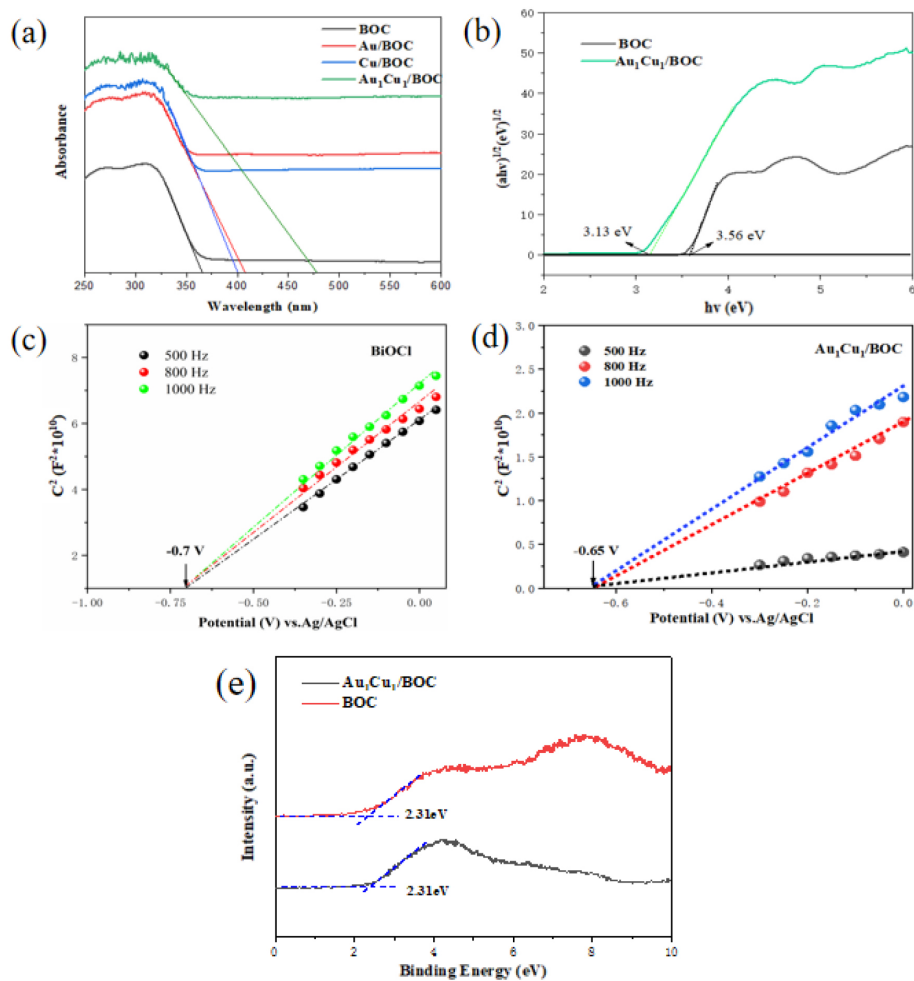

Figure 5. *(a) UV-Vis absorption spectra of photocatalysts. (b) Tauc's plots of pure BiOCl and Au$_1$Cu$_1$/BiOCl. (c) Mott-Schottky plots of pure BiOCl. (d) Mott-Schottky plots of Au$_1$Cu$_1$/BiOCl. (e) Valence-band XPS spectra of pure BiOCl and Au$_1$Cu$_1$/BiOCl samples*

of the Mott-Schottky curve represented by BiOCl is positive, as the basic characteristic of n-type semiconductors is a positive slope; thus, the catalyst is an n-type semiconductor.[40] At measurement frequencies of 500, 800, and 1000 Hz, the derived flat band voltage of BiOCl and Au_1Cu_1/BiOCl are about −0.70 V and −0.65 V (compared to NHE), respectively.[41] Generally speaking, for n-type semiconductors, another characteristic is that their flat band voltage is close to the conduction band voltage. Therefore, it is considered that the conduction band potential of BiOCl is −0.70 V.[42] From the XPS valence band spectrum, pure BiOCl and Au_1Cu_1/BiOCl have the same valence band (2.31 eV), reflecting that when AuCu nanoparticles are deposited on BiOCl nanosheets, the position of the valence band of BiOCl nanosheets remains unchanged (Figure 5d). To calculate the E_{VB} of photocatalysts, we can use the formula $E_g = E_{CB} − E_{VB}$ for calculation. Herein, based on the above formula, the E_{VB} of pure BiOCl and Au_1Cu_1/BiOCl are 2.86 and 2.48 eV.

In order to determine the photoreduced performance of BiOCl, Au/BiOCl, Cu/BiOCl, and Au_xCu_y/BiOCl photocatalysts, we performed photocatalytic CO_2 reduction experiments using a 300 W Xenon lamp under gas-solid conditions without the use of sacrificial agents or photosensitizers. For pure BiOCl, CO was the prime product of photoreduction, and no C_{2+} product was generated (Figure 6a). After 3 h of light irradiation, the CO production rate reached 18.8 μmol h^{-1} g^{-1}. In the case of Cu/BiOCl, CH_4 was generated (1.0 μmol h^{-1} g^{-1}), while the yield of CO decreased from 18.8 to 15.4 μmol h^{-1} g^{-1}. Interestingly, in the case of Au/BiOCl, not only CH_4 was produced (2.3 μmol h^{-1} g^{-1}), but C_2H_6 was also produced (5.4 μmol h^{-1} g^{-1}), with a CO yield of 16.0 μmol h^{-1} g^{-1}. With the introduction of the second metal Cu, the CO yield of the bimetallic Au_xCu_y/BiOCl photocatalysts further decreased, while the yield of CH_4 and C_2H_6 significantly increased. When a small amount of Cu was deposited on Au/BiOCl, and the mass ratio of Au to Cu was 4:1, the photocatalytic performance of the $Au_{1.6}Cu_{0.4}$/BiOC catalyst did not significantly improve. The yield of CO was about 13.6 μmol h^{-1} g^{-1}, the yield of CH_4 decreased to 1.6 μmol h^{-1} g^{-1}, and the yield of C_2H_6

increased from 5.4 to 6.5 μmol h^{-1} g^{-1}. When the quality of Au and Cu was the same, in the Au_xCu_y/BiOCl photocatalysts, Au_1Cu_1/BiOCl had the highest C_2H_6 yield (12.2 μmol h^{-1} g^{-1}), which was 2.3 times that of Au/BiOCl. The CH_4 yield reached 2.93 μmol h^{-1} g^{-1}, and the selectivity of alkane ($CH_4 + C_2H_6$) and C_2H_6 was 88.0 and 77.3%, respectively. Further improving the quality of Cu, when the mass ratio of Au to Cu was 1:4, the photocatalytic performance of the $Au_{0.4}Cu_{1.6}$/BiOC catalyst began to decrease, but it was higher than that of the $Au_{1.6}Cu_{0.4}$/BiOC catalyst. The CO yield was about 13.8 μmol g^{-1} h^{-1}, the CH_4 yield was 2.5 μmol g^{-1} h^{-1}, and the C_2H_6 yield decreased from 12.2 to 7.1 μmol g^{-1} h^{-1}. When a small amount of Cu is deposited, and the amount of Au nanoparticles is excessive, the excessive Au nanoparticles are prone to aggregation during the photodeposition process, ultimately inhibiting the photocatalytic activity of the catalyst. When the quality of Au and Cu is the same, the formation of AuCu alloy enhances the stability of the metal and improves the photocatalytic performance of the catalyst. When a large amount of Cu is deposited, and there are fewer Au nanoparticles, the nanoparticles are less likely to aggregate.[43] The experimental results show that the mass ratio of Au to Cu affects the activity and selectivity of C_{2+} products. In addition, the CO_2 photoreduction performance of Au_1Cu_1/BiOCl was compared with other photocatalysts mentioned in the literature (Table 1). It can be seen that the C_2H_6 formation rate (12.2 μmol h^{-1} g^{-1}) in this work is significantly better than that in recent CO_2 photoreduction studies.

Figure 6b shows the effect of different experimental conditions on the photocatalytic reduction of CO_2. First, we used Ar gas to replace CO_2 gas in the reactor. After 3 h of reaction, no CO product was detected, confirming that CO_2 is the only carbon source for CO reduction. We then performed experiments in a dark environment and without a catalyst, and still could not detect the presence of CO. Therefore, we speculate that the necessary conditions for implementing photocatalytic reactions are: light (light source), catalyst, and CO_2 gas. At the same time, the stability of a photocatalyst is an important parameter to evaluate whether it can be used in
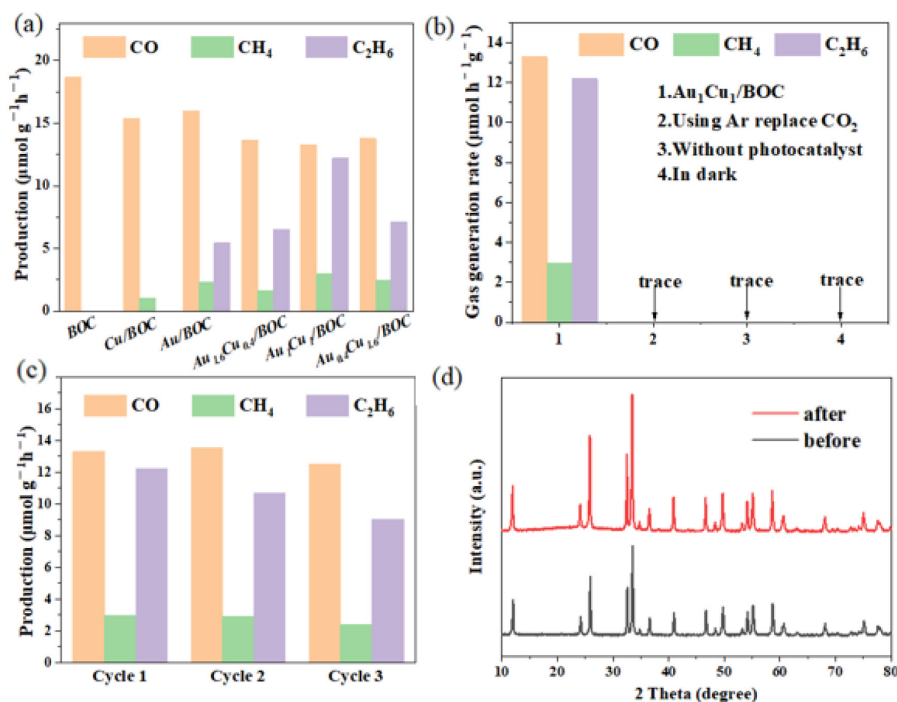
Figure 6. (a) CH_4, C_2H_6, and CO production rates over different photocatalysts after 3 h sunlight (AM 1.5 G) irradiation. (b) The obtained gas products over Au_1Cu_1/BiOCl under different conditions. (c) Photocatalytic stability of Au_1Cu_1/BiOCl. (d) XRD pattern of Au_1Cu_1/BiOCl before and after photocatalytic CO_2 reduction experiment

Table 1. Summary of the photocatalytic conversion of CO_2 to CH_4/CO by different photocatalysts

Photocatalysts	Reaction condition	Formation rate ($\mu mol\ g^{-1}\ h^{-1}$)			Reference
		CO	CH_4	C_2H_6	
Cu/CeO$_{2-x}$NPs	50 mg photocatalyst illuminated using 300 W Xenon-arc lamp	1.7	–	–	44
Cu SAs/g-C$_3$N$_4$	25 mg photocatalyst illuminated using 300 W Xenon-arc lamp	3.1	–	–	45
Cu SAs/TiO$_2$	100 mg photocatalyst illuminated using 300 W Xenon-arc lamp	3.2	–	–	46
Au/TiO$_2$ NPs	100 mg photocatalyst illuminated using 300 W Xenon-arc lamp	–	2.5	1.7	47
Au-Pd alloy/TiO$_2$	10 mg photocatalyst illuminated using 300 W Xenon-arc lamp	–	2.7	–	48
Nanorattle Au@PtAg-ZIF-8	10 mg photocatalyst illuminated using 500 W Xenon-arc lamp	14.5	1.2	–	49
Pd$_7$Cu$_1$/TiO$_2$ NPs	5 mg photocatalyst illuminated using 300 W Xenon-arc lamp (AM 1.5 G)	–	19.6	–	50
Cu-Pt alloy/TiO$_2$	0.4 mg photocatalyst illuminated using 150 W Xenon-arc lamp	–	11.3	–	51
CdS$_{1.5}$/BiOCl-001	50 mg photocatalyst illuminated using 300 W Xenon-arc lamp	0.5	1.71	–	52
1.0%-Au/BOC	30 mg photocatalyst illuminated using 300 W Xenon-arc lamp	43.16	5.98	–	53
Bi/BiOCl-NS	20 mg photocatalyst illuminated using 300 W Xenon-arc lamp	4.75	0.45	–	54
Au$_1$Cu$_1$/BOC	5 mg photocatalyst illuminated using 300 W Xenon-arc lamp (AM 1.5 G)	13.28	2.93	12.2	This work

industrialization, and it is also a criterion for judging the superiority of a catalyst. As can be seen from Figure 6c, Au$_1$Cu$_1$/BiOCl can maintain a relatively stable product yield after three cycles of reaction for 9 h, indicating that the activity of the catalyst has certain stability and repeatability. In addition, Figure 6d shows that after 9 h of photocatalytic reaction, the crystal structure of Au$_1$Cu$_1$/BiOCl was tested again using XRD. It can be seen that the characteristic diffraction peaks of the catalyst before and after the cycle test are the same, reflecting the high recyclability and stability of the catalyst.

In conclusion, the potential mechanism of Au$_1$Cu$_1$/BiOCl composites for photocatalytic CO_2 reduction under sunlight (AM 1.5 G) irradiation is presented in Figure 7. When light shines on the BiOCl nanosheets, it generates photogenerated charges inside the catalyst, namely photogenerated electrons and holes. Compared with BiOCl nanosheets, the work function of Au and Cu is higher; thus, electrons will be transferred from BiOCl nanosheets to gold-copper nanoparticles. AuCu nanoparticles have a special local surface SPR effect, which significantly enhances the absorption of visible light by the catalyst. More importantly, AuCu nanoparticles can be used as "electron traps" to achieve efficient charge transfer. The Au$_1$Cu$_1$/BiOCl composite structure significantly improves the ability

of the catalyst to capture photogenerated electrons, thereby avoiding the electron-hole recombination caused by electrons returning to the valence band.

CONCLUSIONS

In conclusion, bimetallic AuCu nanoparticle BiOCl nanosheets were successfully prepared. AuCu nanoparticles have a special surface plasmon resonance effect, which enhances the catalytic activity of the catalyst, improves the separation efficiency of photogenerated carriers, and realizes efficient charge transfer. As a result, compared with pure BiOCl nanosheets and many reported materials, the prepared composites can generate more valuable C_2H_6 during the photocatalytic reduction process. Au$_1$Cu$_1$/BiOCl has a C_2H_6 yield of 12.2 $\mu mol\ h^{-1}g^{-1}$ and a C_2H_6 selectivity of 77.3%.

AUTHOR CONTRIBUTION

X. Z. and S. W. contributed equally to this work; X. Z. and S. W. were responsible for writing-original draft preparation; X. Z. for investigation; J. Y. for writing-review and editing.
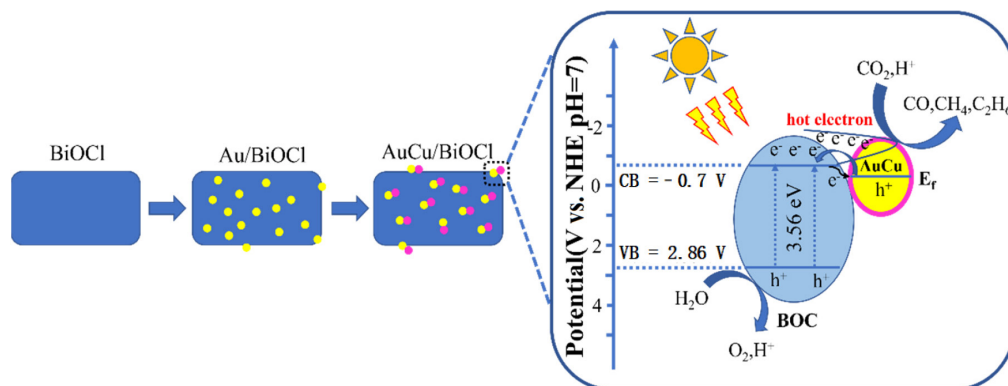
Figure 7. *Illustration of the transfer process of the photogenerated electrons and holes in AuCu/BiOCl during the photocatalytic CO_2 reduction process*

REFERENCES

1. Wang, Y.; Wang, S.; Lou, X. W.; *Angew. Chem., Int. Ed.* **2019**, *58*, 17236. [Crossref]
2. Xiong, J.; Song, P.; Di, J.; Li, H.; *Appl. Catal., B* **2019**, *256*, 117788. [Crossref]
3. Ran, J.; Jaroniec, M.; Qiao, S. Z.; *Adv. Mater.* **2018**, *30*, 1704649. [Crossref]
4. Sorcar, S.; Thompson, J.; Hwang, Y.; Park, Y. H.; Majima, T.; Grimes, C. A.; Durrant, J. R.; In, S. I.; *Energy Environ. Sci.* **2018**, *11*, 3183. [Crossref]
5. Zhao, L.; Ye, F.; Wang, D.; Cai, X.; Meng, C.; Xie, H.; Zhang, J.; Bai, S.; *ChemSusChem* **2018**, *11*, 3524. [Crossref]
6. Jiang, Y.; Long, R.; Xiong, Y.; *Chem. Sci.* **2019**, *10*, 7310. [Crossref]
7. Attri, P.; Garg, P.; Chauhan, M.; Singh, R.; Sharma, R. K.; Kumar, S.; Lim, D. K.; Chaudhary, G. R.; *J. Environ. Chem. Eng.* **2023**, *11*, 109498. [Crossref]
8. Ye, L.; Jin, X.; Ji, X.; Liu, C.; Su, Y.; Xie, H.; Liu, C.; *Chem. Eng. J.* **2016**, *291*, 39. [Crossref]
9. Wang, Y.; Zhao, J.; Liu, Y.; Liu, G.; Ding, S.; Li, Y.; Xia, J.; Li, H.; *J. Colloid Interface Sci.* **2022**, *616*, 649. [Crossref]
10. Stamenkovic, V. R.; Mun, B. S.; Arenz, M.; Mayrhofer, K.; Lucas, C. A.; Wang, G.; Ross, P. N.; Markovic, N. M.; *Nat. Mater.* **2007**, *6*, 241. [Crossref]
11. Takanabe, K.; Nagaoka, K.; Nariai, K.; Aika, K.; *J. Catal.* **2005**, *232*, 268. [Crossref]
12. Wang, A. Q.; Chang, C. M.; Mou, C. Y.; *J. Phys. Chem. B* **2005**, *109*, 18860. [Crossref]
13. Hung, S. F.; Yu, Y. C.; Suen, N. T.; Tzeng, G. Q.; Tung, C. W.; Hsu, Y. Y.; Hsu, C. S.; Chang, C. K.; Chan, T. S.; Sheu, H. S.; Lee, J. F.; Chen, H. M.; *Chem. Commun.* **2016**, *52*, 1567. [Crossref]
14. Lou, Z.; Fujitsuka, M.; Majima, T.; *ACS Nano* **2016**, *10*, 6299. [Crossref]
15. Wang, F.; Jiang, Y.; Lawes, D. J.; Ball, G. E.; Zhou, C.; Liu, Z.; Amal, R.; *ACS Catal.* **2015**, *5*, 3924. [Crossref]
16. Neatu, S.; Macia-Agullo, J. A.; Concepcion, P.; Garcia, H.; *J. Am. Chem. Soc.* **2014**, *136*, 15969. [Crossref]
17. Liu, P.; Gu, X.; Zhang, H.; Cheng, J.; Song, J.; Su, H.; *Appl. Catal., B* **2017**, *204*, 497. [Crossref]
18. Humphrey, J.; Plana, D.; Celorrio, V.; Sadasivan, S.; Tooze, R. P.; Rodríguez, P.; Fermín, D. J.; *ChemCatChem* **2016**, *8*, 952. [Crossref]
19. Kamimura, S.; Yamashita, S.; Abe, S.; Tsubota, T.; Ohno, T.; *Appl. Catal., B* **2017**, *211*, 11. [Crossref]
20. Tahir, M.; Tahir, B.; Amin, N.; *Appl. Catal., B* **2017**, *204*, 548. [Crossref]
21. Zhou, N.; Polavarapu, L.; Gao, N.; Pan, Y.; Yuan, P.; Wang, Q.; Xu, Q. H.; *Nanoscale* **2013**, *5*, 4236. [Crossref]
22. Miao, S.; Huang, M.; Chen, C.; Hu, W. S.; Wang, S.; Li, B. X.; *Colloids Surf., A* **2023**, *670*, 131584. [Crossref]
23. Liu, M.; Zhou, W.; Wang, T.; Wang, D.; Liu, L.; Ye, J.; *Chem. Commun.* **2016**, *52*, 4694. [Crossref]
24. Sugano, Y.; Shiraishi, Y.; Tsukamoto, D.; Ichikawa, S.; Tanaka, S.; Hirai, T.; *Angew. Chem., Int. Ed.* **2013**, *52*, 5295. [Crossref]
25. Ahlawat, M.; Mittal, D.; Govind Rao, V.; *Commun. Mater.* **2021**, *2*, 114. [Crossref]
26. Mondal, I.; Lee, H.; Kim, H.; Park, J. Y.; *Adv. Funct. Mater.* **2020**, *30*, 1908239. [Crossref]
27. DuChene, J. S.; Tagliabue, G.; Welch, A. J.; Cheng, W. H.; Atwater, H. A.; *Nano Lett.* **2018**, *18*, 2545. [Crossref]
28. Sato, Y.; Naya, S. I.; Tada, H.; *APL Mater.* **2015**, *3*, 104502. [Crossref]
29. Ding, J.; Li, X.; Chen, L.; Zhang, X.; Sun, S.; Bao, J.; Gao, C.; Tian, X.; *J. Mater. Chem. A* **2016**, *4*, 12630. [Crossref]
30. Jiang, T.; Jia, C.; Zhang, L.; He, S.; Sang, Y.; Li, H.; Li, Y.; Xu, X.; Liu, H.; *Nanoscale* **2015**, *7*, 209. [Crossref]
31. Zhan, W. C.; Wang, J. L.; Wang, H. F.; Zhang, J. S.; Liu, X. F.; Zhang, P. F.; Chi, M. F.; Guo, Y. L.; Guo, Y.; Lu, G. Z.; Sun, S. H.; Dai, S.; Zhu, H. Y.; *J. Am. Chem. Soc.* **2017**, *139*, 8846. [Crossref]
32. Kim, T. S.; Choi, H.; Kim, D.; Song, H. C.; Oh, Y.; Jeong, B.; Lee, J.; Kim, K. J.; Shin, J. W.; Byon, H. R.; Ryoo, R.; Kim, Y. H.; *Appl. Catal., B* **2023**, *331*, 122704. [Crossref]
33. Chen, Y.; Wu, Y.; Zhang, Y.; Huang, S.; Lv, H.; Chen, J.; Zhai, Y.; Cheng, J.; Pan, J.; *Chem. Eng. J.* **2022**, *429*, 132140. [Crossref]
34. Zhang, Z.; Wang, Z. L.; An, K.; Wang, J.; Zhang, S.; Song, P.; Bando, Y.; Yamauchi, Y.; Liu, Y.; *Small* **2021**, *17*, 2008052. [Crossref]
35. Yu, Y.; Dong, X. A.; Chen, P.; Geng, Q.; Wang, H.; Li, J.; Zhou, Y.; Dong, F.; *ACS Nano* **2021**, *15*, 14453. [Crossref]
36. Delannoy, L.; Thrimurthulu, G.; Reddy, P. S.; Methivier, C.; Nelayah, J.; Reddy, B. M.; Ricolleau, C.; Louis, C.; *Phys. Chem. Chem. Phys.* **2014**, *16*, 26514. [Crossref]
37. Karunakaran, C.; Abiramasundari, G.; Gomathisankar, P.; Manikandan, G.; Anandi, V.; *J. Colloid Interface Sci.* **2010**, *352*, 68. [Crossref]
38. Di, J.; Xia, J.; Ji, M.; Wang, B.; Yin, S.; Zhang, Q.; Chen, Z.; Li, H.; *Appl. Catal., B* **2016**, *183*, 254. [Crossref]
39. Niazi, Z.; Goharshadi, E. K.; Mashreghi, M.; Jorabchi, M. N.; *Photochem. Photobiol. Sci.* **2021**, *20*, 87. [Crossref]
40. Zhang, G.; Chen, D.; Li, N.; Xu, Q.; Li, H.; He, J.; Lu, J.; *Angew. Chem., Int. Ed.* **2020**, *59*, 8255. [Crossref]
41. Wang, S.; Guan, B. Y.; Lu, Y.; Lou, X.; *J. Am. Chem. Soc.* **2017**, *139*, 17305. [Crossref]
42. Tao, R.; Zhao, C.; Shao, C.; Li, X.; Li, X.; Zhang, J.; Yang, S.; Liu, Y.; *Mater. Res. Bull.* **2018**, *104*, 124. [Crossref]
43. Zeng, D.; Yang, L.; Zhou, P.; Hu, D.; Xie, Y.; Li, S.; Jiang, L.; Ling, Y.; Zhao, J.; *Int. J. Hydrogen Energy* **2018**, *43*, 15155. [Crossref]
44. Wang, M.; Shen, M.; Jin, X.; Tian, J.; Li, M.; Zhou, Y.; Zhang, L.; Li, Y.; Shi, J.; *ACS Catal.* **2019**, *9*, 4573. [Crossref]
45. Li, Y.; Li, B.; Zhang, D.; Cheng, L.; Xiang, Q.; *ACS Nano* **2020**, *14*, 10552. [Crossref]
46. Jiang, Z.; Sun, W.; Miao, W.; Yuan, Z.; Yang, G.; Kong, F.; Yan, T.; Chen, J.; Huang, B.; An, C.; Ozin, G. A.; *Adv. Sci.* **2019**, *6*, 1900289. [Crossref]
47. Tu, W.; Zhou, Y.; Li, H.; Li, P.; Zou, Z.; *Nanoscale* **2015**, *7*, 14232. [Crossref]
48. Chen, Q.; Chen, X.; Fang, M.; Chen, J.; Li, Y.; Xie, Z.; Kuang, Q.; Zheng, L.; *J. Mater. Chem. A* **2019**, *7*, 1334. [Crossref]
49. Su, Y.; Xu, H.; Wang, J.; Luo, X.; Xu, Z. L.; Wang, K.; Wang, W.; *Nano Res.* **2019**, *12*, 625. [Crossref]
50. Long, R.; Li, Y.; Liu, Y.; Chen, S. M.; Zheng, X. S.; Gao, C.; He, C. H.; Chen, N. S.; Qi, Z.; Song, L.; Jiang, J.; Zhu, J. F.; Xiong, Y. J.; *J. Am. Chem. Soc.* **2017**, *139*, 4486. [Crossref]
51. Lee, S.; Jeong, S.; Kim, W. D.; Lee, S.; Lee, K.; Bae, W. K.; Moon, J. H.; Lee, S.; Lee, D. C.; *Nanoscale* **2016**, *8*, 10043. [Crossref]
52. Wang, S. S.; Liang, X.; Lv, Y. K.; Li, Y. Y.; Zhou, R. H.; Yao, H. C.; Li, Z. J.; *ACS Appl. Energy Mater.* **2022**, *5*, 1149. [Crossref]
53. Gong, S.; Rao, F.; Zhang, W.; Hassan, Q. U.; Liu, Z.; Gao, J.; Lu, J.; Hojamberdiev, M.; Zhu, G.; *Chin. Chem. Lett.* **2022**, *33*, 4385. [Crossref]
54. Wu, S.; Wang, J.; Li, Q.; Huang, Z.; Rao, Z.; Zhou, Y.; *Trans. Tianjin Univ.* **2021**, *27*, 155. [Crossref]